Monthly Notices
of the
ROYAL ASTRONOMICAL SOCIETY

MNRAS **488,** 4149–4160 (2019)
Advance Access publication 2019 July 31

doi:10.1093/mnras/stz2015

# The eclipsing accreting white dwarf Z chameleontis as seen with *TESS*

J. M. C. Court [1]★ S. Scaringi [1] S. Rappaport,[2] Z. Zhan,[3] C. Littlefield,[4] N. Castro Segura,[5] C. Knigge,[5] T. Maccarone,[1] M. Kennedy [6] P. Szkody[7] and P. Garnavich[4]

[1]*Department of Physics and Astronomy, Texas Tech University, PO Box 41051, Lubbock, TX 79409, USA*
[2]*Department of Physics, Kavli Institute for Astrophysics and Space Research, M.I.T., Cambridge, MA 02139, USA*
[3]*Department of Earth, Atmospheric, and Planetary Sciences, M.I.T., Cambridge, MA 02139, USA*
[4]*Department of Physics, University of Notre Dame, Notre Dame, IN 46556, USA*
[5]*School of Physics and Astronomy, University of Southampton, University Road, Southampton, SO17 1BJ, UK*
[6]*Jodrell Bank Centre for Astrophysics, School of Physics and Astronomy, The University of Manchester, Alan Turing Building, Oxford Road, Manchester, M13 9PL, UK*
[7]*Department of Astronomy, University of Washington, Seattle, WA 98195-1580, USA*

Accepted 2019 July 11. Received 2019 June 17; in original form 2019 May 15

## ABSTRACT

We present results from a study of *TESS* observations of the eclipsing dwarf nova system Z Cha, covering both an outburst and a superoutburst. We discover that Z Cha undergoes hysteretic loops in eclipse depth – out-of-eclipse flux space in both the outburst and the superoutburst. The direction that these loops are executed in indicates that the disc size increases during an outburst before the mass transfer rate through the disc increases, placing constraints on the physics behind the triggering of outbursts and superoutbursts. By fitting the signature of the superhump period in a flux-phase diagram, we find the rate at which this period decreases in this system during a superoutburst for the first time. We find that the superhumps in this source skip evolutionary stage 'A' seen during most dwarf nova superoutbursts, even though this evolutionary stage has been seen during previous superoutbursts of the same object. Finally, O–C values of eclipses in our sample are used to calculate new ephemerides for the system, strengthening the case for a third body in Z Cha and placing new constraints on its orbit.

**Key words:** eclipses – stars: individual: Z Cha – accretion discs – cataclysmic variables.

## 1 INTRODUCTION

Accreting white dwarfs (AWDs) are astrophysical binary systems in which a star transfers matter to a white dwarf companion via Roche lobe overflow. If the white dwarf is not highly magnetized, material that flows through the inner Lagrange point (L1) follows a ballistic trajectory until it impacts the outer edge of an accretion disc, resulting in a bright spot. Material then flows through the disc towards the white dwarf until eventually being accreted. In so-called 'dwarf nova' AWDs, changes in the flow rate through the accretion disc can take place in the form of 'outbursts' (e.g. Warner 1976; Meyer & Meyer-Hofmeister 1984): dramatic increases in luminosity that persist for time-scales of a few days and recur on time-scales of weeks to years (e.g. Cannizzo, Shafter & Wheeler 1988). The cause of these outbursts is likely a thermal instability in the disc related to the partial ionization of hydrogen (Osaki 1974). Some dwarf nova AWDs also undergo 'superoutbursts' (van Paradijs 1983), longer outbursts believed to be triggered during a normal outburst when the radius of the accretion disc reaches a critical value (e.g. Osaki 1989), at which point the disc undergoes a tidal instability and becomes eccentric. Superoutbursts are characterized by the presence of 'superhumps' in their optical light curves, which are modulations in luminosity with periods close to the orbital period of the system. These superhumps are believed to be caused by geometric effects within an expanded accretion disc (Horne 1984), and in a simplistic model, can be understood as the precession of an elongated accretion disc. Systems that undergo superoutbursts are called SU UMa-type systems after the prototype of these systems, SU Ursae Majoris.

Z Chameleontis (Mumford 1969; hereafter Z Cha) is an SU UMa-type AWD consisting of a white dwarf primary and a red dwarf companion, with a well-constrained orbital period of 1.79 h (Baptista et al. 2002). This system shows both outbursts and superoutbursts and, due to its high inclination angle ($\sim 80^{\circ}$, see Table 1), deep eclipses caused by the red dwarf passing in front of the white dwarf and the accretion disc (Mumford 1971). Due to this property, the parameters of this system are relatively well constrained; in Table 1, we list a number of physical properties of the Z Cha system. This combination of outbursts, superoutbursts, and eclipses makes Z Cha an interesting object with which to probe the evolution of AWDs during these events.

★ E-mail: James.Court@ttu.edu

**Table 1.** A table of the physical parameters of the Z Cha system. Values are from McAllister et al. (2019). See Section 4.1 for discussion regarding the orbital period of the system.

| Parameter | Value | Error |
|---|---|---|
| Mass ratio | 0.189 | 0.004 |
| Inclination | 80.44° | 0.11° |
| WD mass | 0.803 $M_\odot$ | 0.014 $M_\odot$ |
| RD mass | 0.152 $M_\odot$ | 0.005 $M_\odot$ |
| WD radius | 0.01046 $R_\odot$ | 0.00017 $R_\odot$ |
| RD radius | 0.182 $R_\odot$ | 0.002 $R_\odot$ |
| Separation | 0.734 $R_\odot$ | 0.005 $R_\odot$ |

In this paper, we report on *TESS* observations of Z Cha taken during two different intervals in 2018. We describe the observations in Section 2, and our results relating to the timing characteristics of the system in Sections 4.1 and 4.3. Finally, in Section 4.2 we perform a population study of the eclipses observed by *TESS*, and discuss how they change over the course of both an outburst and a superoutburst.

## 2 OBSERVATIONS

The *Transiting Exoplanet Survey Satellite* (*TESS*; Ricker et al. 2009) is a space-based optical telescope launched in 2018. The telescope consists of four cameras, each with a field of view (FOV) of 24° × 24°, resulting in a total telescope FOV of 24° × 96°. Each camera consists of 4096 × 4096 pixels, resulting in an effective resolution of 21 arcsec, and is effective at wavelengths of ∼600–1000 nm.

*TESS*'s primary mission is to perform an all-sky survey to search for transiting exoplanets. This survey is performed by dividing the sky into a number of 'sectors', each of which corresponds to the total field of view of all four cameras. These sectors overlap near the ecliptic poles; as such, many objects have been or will be observed in multiple sectors. Each sector is observed for approximately 27 d at a cadence of 2 min, and a Full Frame Image (FFI) is returned once every 30 min. Due to telemetry constraints, only images of ∼16 000 pre-selected ∼10 × 10 pixel 'Postage Stamps' are returned at the optimum 2 min cadence, creating a Target Pixel File (TPF) for each Postage Stamp. Simple aperture photometry is applied to each of the TPFs to obtain a barycentred Light Curve File (LCF) of a selected object within that TPF. FFIs, TPFs, and LCFs from *TESS* are available at the Mikulski Archive for Space Telescopes[1] (MAST).

Z Cha (Tess Input Catalogue ID 272551828) has been observed during two *TESS* Sectors: Sector 3 between BJDs 2458385 and 2458406 and Sector 6 between BJDs 2458467 and 2458490. We show the LCF-generated Z Cha light curves from these sectors in Figs 1 and 2, respectively. During Sector 3, Z Cha underwent a superoutburst beginning on BJD 2458391 and persisting until at least the end of Sector 3. The initial part of this superoutburst took the form of a normal outburst, transitioning to a superoutburst around BJD ∼ 2458394. During Sector 6, Z Cha underwent a normal outburst beginning on BJD 2458481 and persisting until around BJD 2458486. Both observations include a significant data gap, in each case caused by the Earth rising above the sun-shade on the spacecraft and contributing significant scattered light.[2]

[1] https://archive.stsci.edu/tess/

[2] Data Release Notes (DRNs) on *TESS* Sectors 3 and 6 can be found at https://archive.stsci.edu/tess/tess_drn.html.

## 3 DATA ANALYSIS

To analyse *TESS* data from Sectors 3 and 6, we use our own software libraries[3] to extract data from the native `.fits` LCF files and to create secondary data products such as flux-phase diagrams and power spectra. As the data in *TESS* LCFs are barycentred, and hence not evenly spaced in time, we do not produce Fourier spectra from the data. Instead, we analyse timing properties using the generalized Lomb–Scargle method (Irwin et al. 1989): a modification on Lomb–Scargle spectral analysis (Lomb 1976; Scargle 1982) that weights data points based on their errors. To extract periods from our Lomb–Scargle spectra, we fit Gaussians in the region of the respective peaks in frequency space.

When creating generalized Lomb–Scargle spectra, we first detrend our data to remove long-term variability and trends such as the evolution of an outburst and a superoutburst. To perform this detrending, we subtract a value $N_t$ from each point in our data set. $N_t$ is calculated by taking a window of width 0.074 499 2631 d, or the orbital period of Z Cha (McAllister et al. 2019). The lower and upper quartiles of the flux values of the data within this window are calculated, and all points outside of the interquartile range are discarded. $N_t$ is then defined as the arithmetic mean of the flux values of the remaining points. By discarding all values outside of the interquartile range, we remove the flares and eclipses from our detrending process and ensure that our calculated trend is close to describing how the out-of-eclipse rate of the object changes over time.

### 3.1 Extracting eclipses

To study how the eclipse properties varied as a function of time in each sector, we calculated the time of each eclipse minimum assuming an orbital period of 0.074 499 2631 d (McAllister et al. 2019). We created a new light curve with eclipses removed by removing all data within 0.1 phases (∼0.007 d) of each eclipse minimum. We then fit a spline to the remaining data to fill in the gaps using a uniformly spaced time grid. This eclipse-free light curve could then be subtracted from the original light curve to isolate only the eclipse features. We show some sample resultant light curves from this algorithm in Fig. 3.

We split both the eclipse-removed and eclipse-only light curves into segments of length equal to one orbital period, such that each segment contains the entirety of a single eclipse. We fit a Gaussian to each of these segments. The shape of an eclipse is in general complex, consisting of eclipses of multiple components of the system each with a separate ingress and egress. Therefore, to fit each eclipse, we only fit data less than 0.1 phases before or after the expected eclipse minimum, as the profile of each eclipse is Gaussian-like in this range. We use this fit to extract a number of parameters for each eclipse, including amplitude $-A$, width $\sigma$, and phase $\phi$; we show an example Gaussian fit in Fig. 4. We also estimate the out-of-eclipse count rate $\bar{r}$ for each eclipse by taking the median of the corresponding segment of the eclipse-removed light curve, resulting in a total of four parameters for each eclipse.

A number of small gaps exist in the data set, generally due to anomalous being manually excluded during the light curve processing. Due to these gaps, some eclipses are partially or completely missing from our sample, and hence a Gaussian fit to these segments of the eclipse-only light curve is poorly constrained.

[3] Available at https://github.com/jmcourt/TTU-libraries.

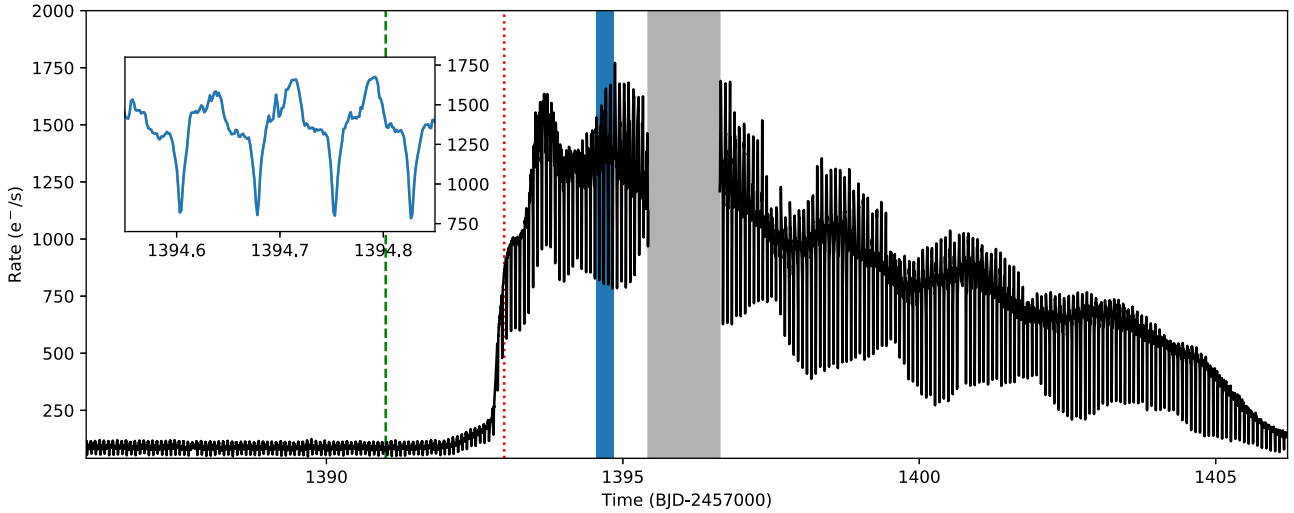


**Figure 1.** The full *TESS* light curve of Z Cha during Sector 3; inset: we plot a zoom in on the region highlighted in blue to show the presence of eclipses. The data gap centred at about BJD 2458396 (highlighted in grey) is due to the telescope being repointed to downlink data to the Earth at this time. Eclipses at BJDs ∼ 2458388 and 2458401 occur during smaller data gaps, and hence appear as 'missing' eclipses in this light curve. The green dashed line at BJD 2458391 represents a conservative estimate of the start time of the superoutburst, which we use to select eclipses that occurred during quiescence (see Section 4.1). The red dotted line at BJD 2458393 represents the approximate onset time of superhumps (see Section 4.3).

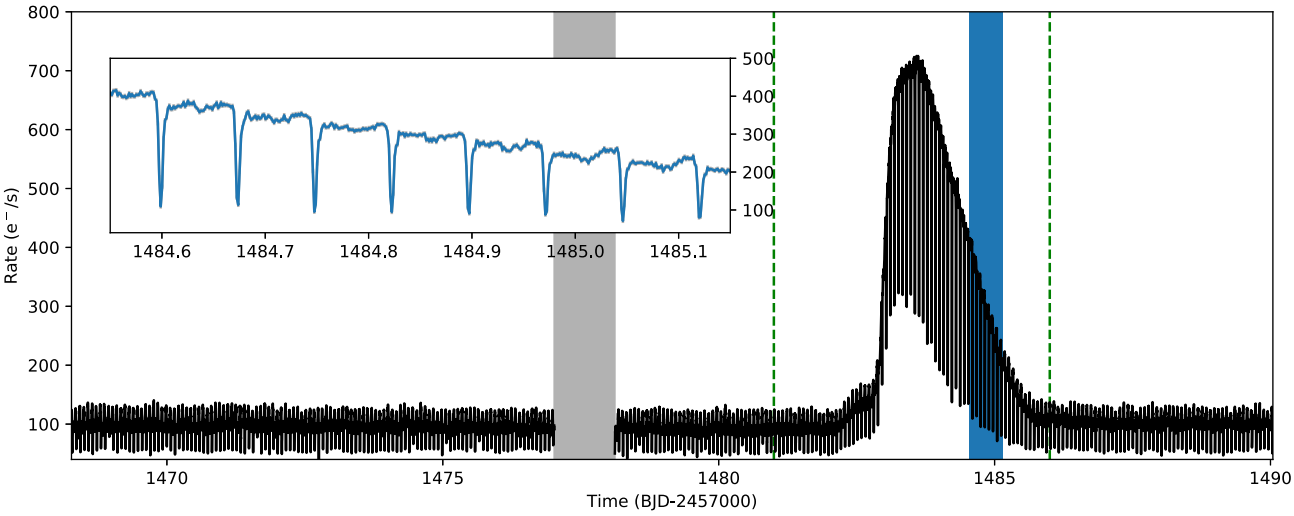


**Figure 2.** The full *TESS* light curve of Z Cha during Sector 6; inset: we plot a zoom in on the region highlighted in blue to show the presence of eclipses. The data gap centred at about BJD 2458477.5 (highlighted in grey) is due to the telescope being repointed to downlink data to the Earth at this time. Eclipses at BJDs ∼ 2458469 and 2458471 occur during smaller data gaps, and hence appear as 'missing' eclipses in this light curve. The green dashed lines at BJDs 2458481 and 2458486 represent conservative estimates of the start and end times of the outburst, which we use to select eclipses that occurred during quiescence (see Section 4.1). Note that the vertical scale on this figure is different to Fig. 1.

To clean our sample, we remove all eclipses for which the magnitude of any of $A$, $\sigma$, or $\bar{r}$ is less than three times the magnitude of the corresponding error.

## 4 RESULTS

In this section, we present the results of the analysis we describe in Section 3. First, we present our new value for the orbital period of Z Cha, as well as new ephemerides for the system based on fits to historical O–C data. Then we present our study of the superhump, presenting a new value for its mean frequency and showing that it does not undergo evolutionary stage A (Kato et al. 2009). Finally, we present our study of the eclipses in this system, showing that hysteresis in max-eclipse-depth–out-of-eclipse-flux space occurs during both the outburst and the superoutburst.

### 4.1 Orbital period

In Figs 5 and 6, we show dynamic power spectra constructed from the data of Sectors 3 and 6, respectively, after removing the outburst profile found using the algorithm described in Section 3. In both the plots, a strong and constant signal at $\nu_0 = 13.428(\pm1)$ c/d can be seen, corresponding to an orbital period of the system $P_{\rm orb} = 0.074\,472(6)$ d.

We calculate an orbital period $P_{\rm orb}$ for the Z Cha system independently using our data set so that our value can be used

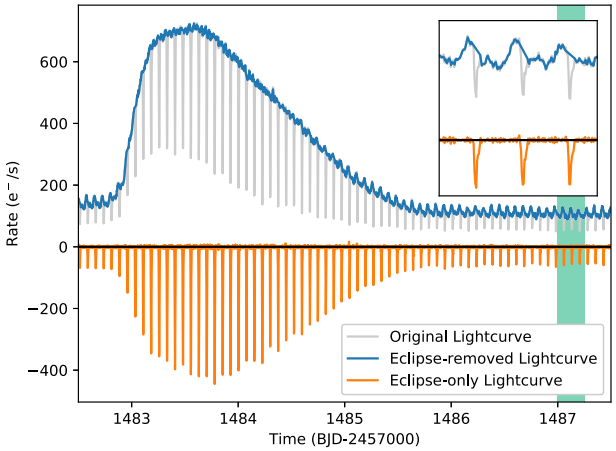


**Figure 3.** The results of applying the algorithm we describe in Section 3.1 to the portion of the Sector 6 light curve of Z Cha containing the outburst. In light grey we show the original light curve, which we have decomposed into an eclipse-removed light curve (blue) and an eclipse-only light curve (orange). Inset: we show a zoom to the period during the light curves highlighted in green. Note that, due to the presence of a pre-eclipse brightening caused by the hotspot coming into view (see also Figs 4 and 7), an amount of orbital modulation is still visible in the eclipse-removed light curve.

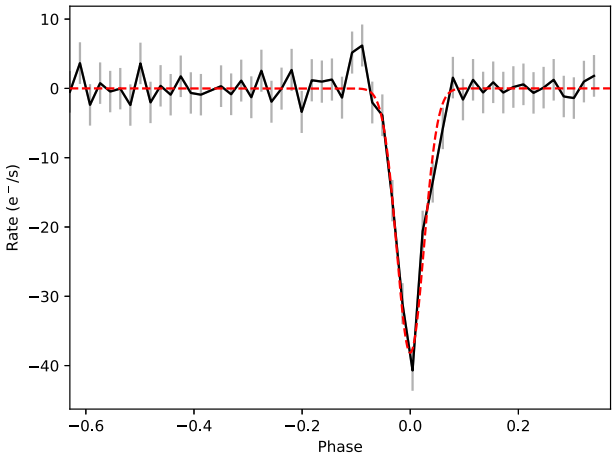


**Figure 4.** The light curve of a typical eclipse in the eclipse-only light curve of Z Cha (black), along with the shape of the Gaussian (red) that we fit to it to extract parameters.

to better constrain the characteristics of the Z Cha system. Starting with the orbital period of 0.074 472 d indicated by our dynamical power spectrum, we calculated the cycle number (since an arbitrary start time) corresponding to each eclipse minimum during portions of the data set in which Z Cha was in quiescence. We then fit a function $t_{\rm min} = P_{\rm orb}N + t_0$ to the eclipse minima times to obtain a value for $P_{\rm orb}$. We obtain an orbital period of 0.074 499 53(5), which is slightly longer than the value of 0.074 499 2631(3) d reported by McAllister et al. (2019). In Fig. 7, we show a portion of the light curve of Sector 6 folded over our value for the orbital period.

We also calculate the O–C values (the difference between observed eclipse time and expected eclipse time according to a given ephemeris) of the eclipses in our sample compared to the linear ephemeris provided by Baptista et al. (2002), which we reproduce in Table 2. Due to the presence of significant variations of the value of $\phi$ in eclipses during the outburst and superoutburst (discussed in more detail in Section 4.2), we do not use any eclipses after BJD 2458391 in Sector 3 or between BJDs 2458481 and 2458486 in Sector 6; these times are marked on Figs 1 and 2. By averaging the O–C values for all eclipses in the remaining periods of quiescence, we find a mean O–C of −293.3(7) s.

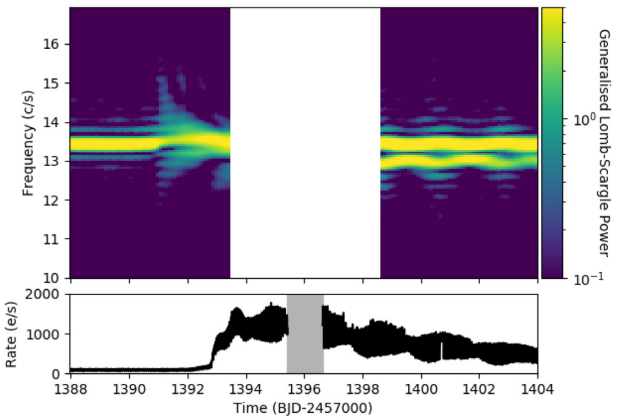


**Figure 5.** A dynamic Lomb–Scargle spectrogram of the Sector 3 observation of Z Cha. Each spectrum corresponds to a 4 d window of data, which is moved 0.1 d at a time. We also show the light curve of Sector 3 on the same *x*-axis for comparison. Note that the dynamic power spectrum is heavily oversampled; using a window size of less than ∼4 d does not allow us to resolve the orbital and superhump periods as separate features.

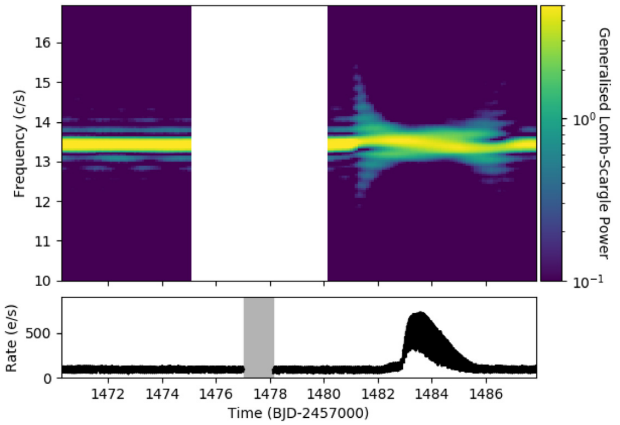


**Figure 6.** A dynamic Lomb–Scargle spectrogram of the Sector 6 observation of Z Cha. Each spectrum corresponds to a 4 d window of data, which is moved 0.1 d at a time. We also show the light curve of Sector 6 on the same *x*-axis for comparison. Note that the dynamic power spectrum is heavily oversampled, consistent with Fig. 5.

We show our O–C value in Fig. 8 alongside O–C values against the Baptista et al. (2002) ephemeris for eclipse times reported in a number of previous studies (Cook 1985; Wood et al. 1986; Honey et al. 1988; Warner & O'Donoghue 1988; van Amerongen, Kuulkers & van Paradijs 1990; Robinson et al. 1995; Baptista et al. 2002; Dai et al. 2009; Nucita et al. 2011; Pilarčík et al. 2018). We choose the ephemeris from Baptista et al. (2002) as a reference due to its linearity.

A number of previous studies (e.g. Baptista et al. 2002) have noted an apparently sinusoidal variation in the O–C values of eclipses in Z Cha. This effect has been seen in other eclipsing AWDs (e.g. Bond & Freeth 1988), and has variously been attributed to either a secular process caused by magnetic cycles in the donor star (the Applegate mechanism, Applegate 1992) or the presence

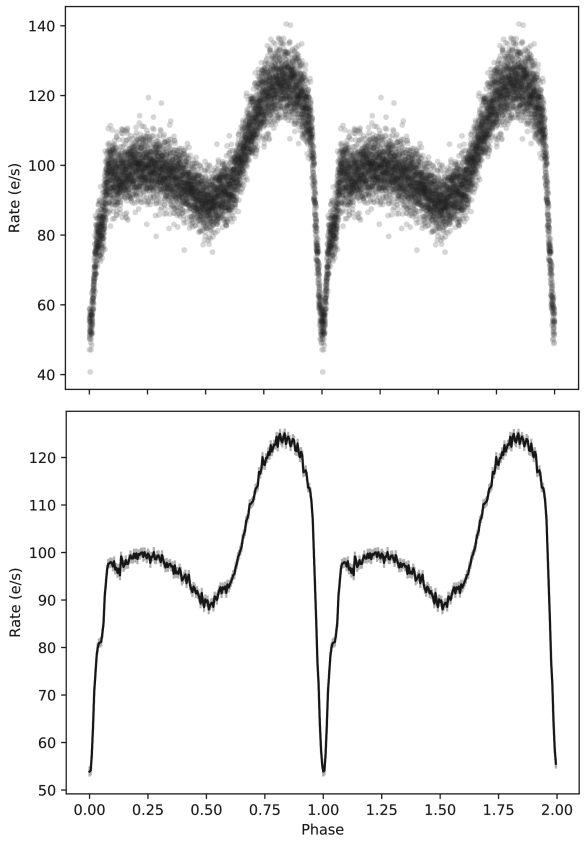


**Figure 7.** Upper: the light curve of data from Sector 6 before the data gap at BJD ∼ 2458477.5, folded over our measured orbital period of 0.074 499 53 d. We choose this segment of our data to fold here as the out-of-eclipse intensity of Z Cha changes little during this interval, and hence the shape of the average eclipse can be better seen. Lower: the same folded light curve, rebinned into phase bins of width 0.005, to better show fine features of the mean cycle such as the egress of the hotspot at $\phi \sim 0.1$.

of a third body in the system. In the latter scenario, this third body either periodically transfers angular momentum to the visible components, or causes a periodic shift in the distance, and hence light-traveltime, to the visible components. Dai et al. (2009) note that the Applegate mechanism cannot be employed to satisfactorily explain the variations in the orbital period of Z Cha. Consequently, previous authors (e.g. Baptista et al. 2002; Dai et al. 2009) have fitted ephemerides with a sinusoidal component to the archival eclipse times of Z Cha, in order to extract the orbital characteristics of the hypothetical third body. In Fig. 8, we also show the expected O–C values for sinusoidal ephemerides calculated in Baptista et al. (2002) and Dai et al. (2009), as well as a quadratic ephemeris presented in Robinson et al. (1995); in each case, our new data point lies far outside the confidence region associated with the respective ephemeris.

We calculate a new ephemeris for Z Cha by fitting a function to all the eclipse time data with the form

$$t_e = T_0 + P_0 N + A \sin\left(\frac{2\pi(t_e - T_1)}{P_1}\right)$$
$$\approx T_0 + P_0 N + A \sin\left(\frac{2\pi(T_0 + P_0 N - T_1)}{P_1}\right) \quad (1)$$

assuming $A \ll P_0 N$.

**Table 2.** A table of ephemerides for the eclipses of Z Cha for which we simulate O–C values in Fig. 8. In each case, $t_e$ is the expected time of minimum light of the $N^{th}$ eclipse since some time $T_0$.

| |
|---|
| Baptista et al. (2002) linear ephemeris |
| $t_e = T_0 + P_0 N$ |
| $T_0 = 2440\,264.680\,70(\pm4)$ d |
| $P_0 = 0.074\,499\,3048(\pm9)$ d |
| Robinson et al. (1995) quadratic ephemeris |
| $t_e = T_0 + P_0 N + cN^2$ |
| $T_0 = 2440\,264.632\,13(\pm9)$ d |
| $P_0 = 0.074\,499\,2575(\pm24)$ d |
| $c = 3.77(\pm6)$ d |
| Baptista et al. (2002) sinusoid ephemeris |
| $t_e = T_0 + P_0 N + A\cos(2\pi(N - B)/C)$ |
| $T_0 = 2440\,264.6817(\pm1)$ d |
| $P_0 = 0.074\,499\,297(\pm2)$ d |
| $A = (7.2 \pm 1.0) \times 10^{-4}$ d |
| $B = (120 \pm 4) \times 10^{3}$ |
| $C = (136 \pm 7) \times 10^{3}$ |
| Dai, Qian & Fernández Lajús (2009) sinusoid ephemeris |
| $t_e = T_0 + P_0 N + A\sin(2\pi BN + C)$ |
| $T_0 = 2440\,265.85(2)$ d |
| $P_0 = 0.074\,499\,293(4)$ d |
| $A = (8.8 \pm 0.1) \times 10^{-4}$ d |
| $B = (2.4 \pm 3) \times 10^{-5}$ |
| $C = (0.992 \pm 7) \times 10^{3}$ |

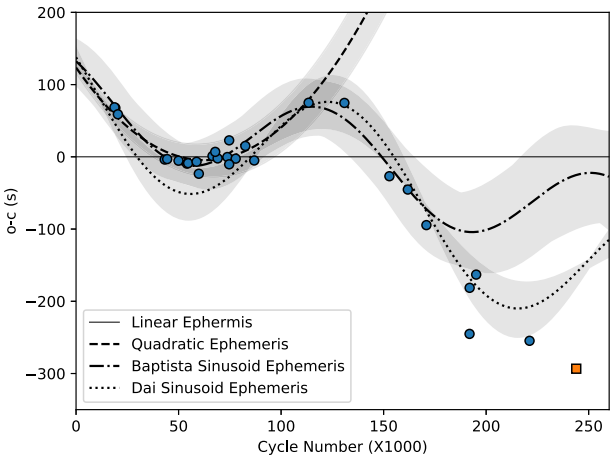


**Figure 8.** A plot of the O–C values for reported eclipse times against the linear ephemeris of Baptista et al. (2002) over time. The blue points are recalculated O–C values for eclipses reported in the literature (see the main body of text for sources), whereas the orange square represents the point added by our study. In the black lines, we plot the expected O–C values for a number of different ephemerides; see Table 2 for further details. The grey area associated with each black line represents the $1\sigma$ confidence interval associated with that ephemeris.

We rebin the arrival times into observing runs: periods of time of at most a few days in which the separation between observations is much less than the separation from the next and previous runs. The error of each of these runs is taken to be the value of its rms scatter; when fitting, we weight each run by the reciprocal square root of this value. If this error is smaller than 10 s, we increase it to 10 s to attempt to account for historical systematic errors. If a run contains

**Table 3.** A table of the new best-fitting linear and sinusoid ephemerides that we calculate for eclipses in Z Cha.

| New linear ephemeris |
|---|
| $t_e = T_0 + P_0 N$ |
| $T_0 = 2440\,000.060\,88(7)$ d |
| $P_0 = 0.074\,499\,2878(4)$ d |
| **New sinusoid ephemeris** |
| $t_e = T_0 + P_0 N + A \sin\left(\frac{2\pi(T_0+P_0N-T_1)}{P_1}\right)$ |
| $T_0 = 2440\,000.060\,88(7)$ d |
| $P_0 = 0.074\,499\,2878(4)$ d |
| $A = 0.000\,92(5)$ d |
| $T_1 = 2446\,781 \pm 140$ d |
| $P_1 = 13\,550 \pm 438$ d |

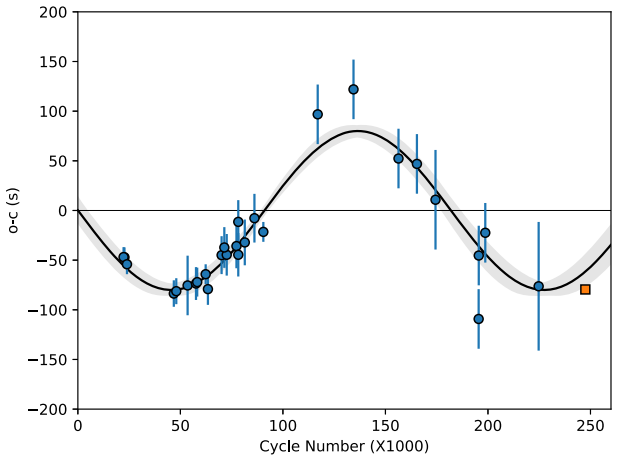


**Figure 9.** A plot of the O–C values for reported eclipse times against our new linear ephemeris (see Table 3) over time. The blue points are recalculated O–C values for eclipses reported in the literature (see the main body of text for sources), whereas the orange square represents the point added by our study. In the black lines, we plot the expected O–C values from our new sinusoid ephemeris (also in Table 3). The grey area represents the $1\sigma$ confidence interval associated with our ephemeris.

only 1 point, we assume a conservative error of 30 s. Even after doing this, the O–C values from historical data must be treated with caution, as a number of different standards for converting times to BJD exist and it is not always clear which is being used by a given author. These different standards can lead to differences in reported eclipse times of the order of ∼50 s (e.g. van Amerongen et al. 1990; Eastman, Siverd & Gaudi 2010) and we do not attempt to correct for them here.

We present the results of fitting equation (1) to our data set in Table 3, and in Fig. 9 we show how it fits the O–C taken against a new best-fitting linear ephemeris (also given in Table 3). These values suggest that the orbit of the speculative third body in the Z Cha system has an orbital period of $37.5 \pm 0.5$ yr. We find that the main components of Z Cha likely orbit the centre of mass common to this third body with a semimajor axis of $>82.2 \pm 5$ light-seconds [35.4(2) $R_\odot$] depending on the inclination angle.

### 4.2 Eclipse properties

As we do not fix the phase when fitting Gaussians to each eclipse, the phase $\phi$ at which minimum light occurs is free to vary slightly from

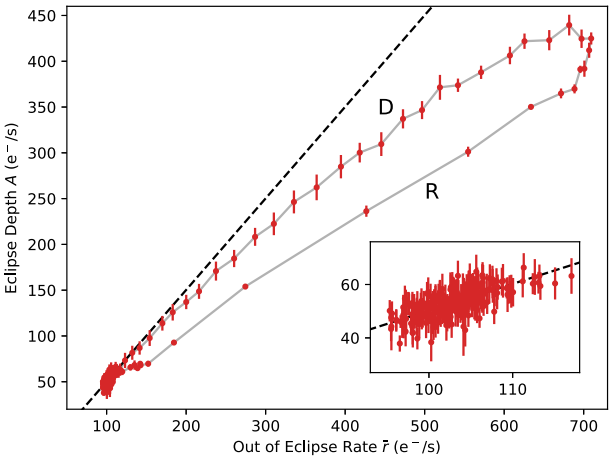


**Figure 10.** A plot of eclipse amplitude $A$ against out-of-eclipse rate $\bar{r}$ (an eclipse fraction diagram) for all well-constrained eclipses in the Sector 6 *TESS* observation of Z Cha. The data points are joined sequentially by a grey line to show evidence of hysteresis during the outburst; the track traced by eclipses during the rise (decay) of the outburst is labelled **R** (**D**). The black line is a line with gradient = 1 fit to the data points corresponding to eclipses during quiescence; inset: we show a zoom to the eclipses used to calculate this line.

eclipse to eclipse. We find that, indeed, the minimum-light phase indicated by our fitting does show small but significant variations of the order of $0.01\,\phi$, especially shortly after the onset of both the outburst and the superoutburst. This effect has previously been noted by Robinson et al. (1995), who attribute the phase jump during outbursts to be due to each eclipse consisting of a hybrid event: an eclipse of the hotspot and an eclipse of the disc that cannot be cleanly separated. The effect has also been noted in a number of other eclipsing AWDs, including V447 Lyrae (Ramsay et al. 2012) and CRTS J035905.9+175034 (Littlefield et al. 2018).

In other eclipsing AWDs such as GS Pav (Groot et al. 1998) and KIS J192748.53+444724.5 (Scaringi, Groot & Still 2013), it has been shown that, during quiescence, the depth of an eclipse shows a linear correlation with the out-of-eclipse luminosity. The gradient of this relationship is very close to unity, which is interpreted as being due to same fraction of the accretion disc flux being obscured during each eclipse. However, when these systems undergo outbursts, the eclipse depths deviate from this relationship and become shallower. This is interpreted as being due to a combination of the radial temperature gradient of the disc changing and the physical size of the disc; in each case, the donor star will eclipse a smaller fraction of the integrated luminosity during each eclipse, and hence the eclipses become shallower than would be expected from the 1:1 relation.

In Fig. 10, we show a plot of eclipse amplitude $A$ against out-of-eclipse rate $\bar{r}$ (hereafter, referred to as an 'eclipse fraction diagram') for all eclipses in the Sector 6 *TESS* observation of Z Cha, which includes a normal outburst. To check that the expected 1:1 relationship between $A$ and $\bar{r}$ is consistent with our observations, we fit a $y = mx + c$ curve to the portion of these data corresponding to quiescence (e.g. before and after the outburst start and end times, marked with the dashed green lines in Fig. 2). We find $m = 0.93 \pm 0.07$. As this is consistent with 1, we set $m = 1$ and fit a $y = x + c$ curve to our data (black line in Fig. 10), obtaining an $x$-intercept of $49.8(3)\,e^-\,s^{-1}$. This intercept gives the out-of-eclipse flux of the system when the eclipse depth is 0, i.e. there is no disc to eclipse. As such, this value gives an estimate for the flux of the donor star, and it should be constant across all outbursts of Z Cha.

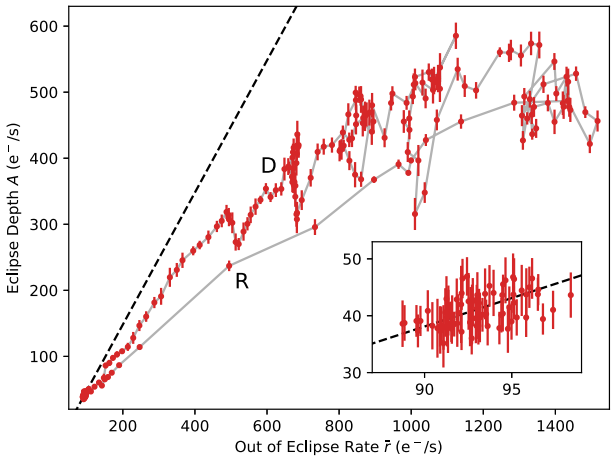


**Figure 11.** A plot of eclipse amplitude $A$ against out-of-eclipse rate $\bar{r}$ (an eclipse fraction diagram) for all well-constrained eclipses in the Sector 3 *TESS* observation of Z Cha, which includes the superoutburst. The data points are joined sequentially by a grey line to show evidence of hysteresis during the outburst; the track traced by eclipses during the rise (decay) of the outburst is labelled **R** (**D**). The black line is a line with gradient = 1 fit to the data points corresponding to eclipses during quiescence; inset: we show a zoom to the eclipses used to calculate this line.

We also show that eclipses during the outburst in Sector 6 exhibit the same behaviour as those seen in other eclipsing AWDs, in that their $A$-values dip below the 1:1 relationship with $\bar{r}$ during an outburst. In addition to this, we find strong evidence of hysteresis in this parameter space during the outburst; during the rise of the outburst, eclipses move along a track at lower eclipse depth $A$ (track **R**, marked in Fig. 10) and then return to quiescence along a track at higher $A$ (track **D**). As the eclipses in our sample are approximately equally spaced in time, the sparsity of points along track **R** compared to track **D** indicates that movement along track **R** is completed in a significantly shorter time. Hysteresis in this parameter space during a dwarf nova outburst has previously been noted by Scaringi et al. (2013).

In Fig. 11, we show the eclipse fraction diagram for all eclipses in Sector 3, including the superoutburst. We again check the 1:1 correlation between these parameters by fitting a $y = mx + c$ line to the data during quiescence, and obtain a gradient $m = 0.7 \pm 0.2$. This figure is more than $1\sigma$ lower than 1, although the line is not very well constrained ($c = -28 \pm 16\,\mathrm{e^-\,s^{-1}}$) due to the relatively low number of quiescent eclipses in Sector 3 (72) compared to Sector 6 (220). If we again fix the gradient to 1 and refit the line, we obtain an $x$-intercept $c = 51.9 \pm 0.3\,\mathrm{e^-\,s^{-1}}$. This is significantly different from the $x$-intercept, and hence donor star flux, that we obtain by fitting a straight line to the quiescent periods in Sector 6. This in turn further suggests that a 1:1 fit to the data in Sector 3 is not physical.

Again we find evidence of hysteresis, confirming that the hysteresis reported by Scaringi et al. (2013) during dwarf nova outbursts can also occur during superoutbursts. Again, the hysteresis generally consists of two tracks: an outbound track **R** that is completed in relatively little time, and a decay track **D** that occurs at generally higher values of $A$ than on track **R**. The hysteresis in Fig. 11 appears somewhat more complicated than that in Fig. 10, but some of the excursions to high or low values of $A$ along path **D** are likely due to the superhump modulation, causing us to periodically overestimate $A$.

### 4.3 Superhump

In Fig. 5, a second signal is also visible peaking at a mean frequency of $\sim$12.95 d$^{-1}$, or a period of 0.077 13($\pm$7) d. This signal is only visible during the superoutburst portion of Sector 3, and is absent from all of Sector 6 including the outburst, and so we identify this feature as a 'positive superhump': a modulation of the disc caused by its geometric elongation and subsequent precession after it extends beyond the 3:1 resonance point with the companion star (e.g. Wood et al. 2011). The superhump begins on BJD $\sim$ 2458393, less than 3 d before the start of the data gap and at the approximate time of the transition of an outburst into the superoutburst. Due to the data gap centred around BJD 2458396, and the end of the observation, the early- and late-time evolution of the superhump is lost. Towards the end[4] of the observation at BJD $\sim$ 2458404, the amplitude of the superhump begins to weaken significantly, at the same time that the superoutburst is beginning to end (see e.g. Fig. 1 for comparison).

A positive superhump has previously been reported in Z Cha by Kato et al. (2015) during a 2014 superoutburst of the source. They calculated the mean period of the superhump as 0.077 36(8) d during the dominant evolutionary Stage B (see Kato et al. 2009). Using bootstrapping to estimate errors, we calculate a mean superhump period of 0.077 13($\pm$7) d from our data set, somewhat shorter than that calculated by Kato et al. This discrepancy may in part be due to sampling effects, as the superhump period changes significantly during the course of Stage B.

Studies of superhumps in other SU UMa-type systems have found 'fading' events during superoutburst, in which the system becomes a few tenths of a magnitude fainter for $\sim$1 d before rebrightening (Littlefield et al. 2018). We see similar features during the superoutburst of Z Cha in the form of an $\sim$2 d modulation in flux apparent in Fig. 1. However, this modulation occurs very close to the beat period between the orbital period and the mean superhump period ($\sim$2.13 d), and hence is likely an artefact of this beat. As the positive superhump is generally interpreted as occurring at the beat frequency of the disc precession and the orbital period (Hellier 2001), this 2.13 d period may also be interpreted as the synodic precession period of the elongated accretion disc during superoutburst.

The modulation that causes the superhump can also be readily seen in the light curve. In Fig. 12, we show a flux-phase diagram of the light curve from the Sector 3 observation of Z Cha, in which the light curve has been folded over the orbital period of the system and then stacked vertically. This diagram shows how the phase of a periodic or quasi-periodic event changes with time. The brightening events associated with the superhump can clearly be seen as 'diagonal lines' in this plot, arriving slightly later during each orbital period due to the superhump's period being slightly greater than that of the orbit. In Fig. 13, we show a similar flux-phase diagram, this time folded over the mean period that we calculated for the superhump. Including the 10 cycles that occur before the data gap, the superhump appears as a parabola-like shape in this plot; at first, it arrives later than its expected time of arrival, but this delay decreases over time and eventually reverses, indicating that the period of the superhump is decreasing over time.

[4]The data for our dynamic Lomb–Scargle periodograms end 2 d before the end of the associated light curve data due to our choice of a 4 d window when producing Lomb–Scargle periodograms.

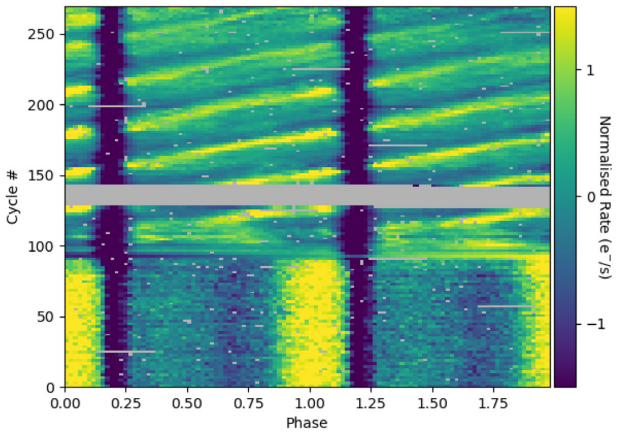


**Figure 12.** A flux-phase plot of the Sector 3 light curve of Z Cha; a light curve that has been cut into segments equal to two times the orbital period and then stacked vertically, to show how light curve morphology varies as a function of cycle number. The brightening associated with the superhump can be seen as diagonal tracks. The count rates in each orbit have been converted to 'normalized rate' by subtracting the mean and dividing by the standard deviation. The horizontal grey regions correspond to data gaps.

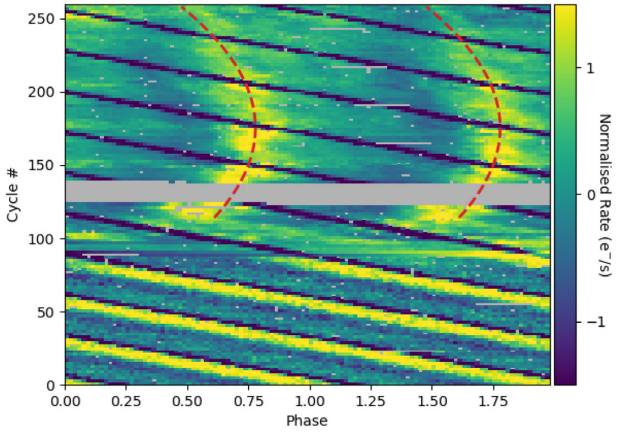


**Figure 13.** A flux-phase plot of the Sector 3 light curve of Z Cha, folded on the mean superhump period we calculated. The count rates in each orbit have been converted to 'normalized rate' by subtracting the mean and dividing by the standard deviation. In red, we plot the parabola we fit to the central superhump phase as a function of time (see Table 4). The horizontal grey regions correspond to data gaps.

## 5 DISCUSSION

### 5.1 Third body in the Z Cha system

Sinusoidal O–C modulations have been identified or proposed in a number of additional AWD systems (e.g. Bond & Freeth 1988; Dai et al. 2010; Han et al. 2016), but the orbital cycles of these systems are generally either poorly sampled or have not been observed in their entirety. Previous studies have shown that these modulations cannot always be explained by the orbit of a third body (e.g. Bianchini et al. 2004); instead they suggest secular processes such as the Applegate mechanism (Applegate 1992), in which the donor star is periodically deformed due to its own magnetic activity and this deformation is coupled with a redistribution of angular momentum in the system. Dai et al. (2009) have previously attempted to use the Applegate mechanism to explain the O–C modulation seen in Z Cha. They calculated the minimum energy required to redistribute sufficient angular momentum in the companion star via this effect to reproduce the observed amplitude of the oscillation. They found that the required energy was ∼1 order of magnitude greater than the entire energy output of the star over an oscillation period, and hence ruled out the Applegate mechanism as the driver of this oscillation (see also Brinkworth et al. 2006, for a full treatment of the energetics of the Applegate mechanism). We find a sinusoid amplitude of 79.5 ± 4 s; as this number is similar to value of ∼90 s obtained by Dai et al., we find that the energetic output of the donor star is still much too small to explain the O–C modulation via the Applegate mechanism. As such, our results further strengthen the case for the presence of a low-mass third body in Z Cha (see also studies by, e.g. Baptista et al. 2002).

If the sinusoidal modulation in O–C is caused by a light-traveltime effect, we calculate an orbital period for this body of 37 ± 0.5 yr, similar to the recent orbital period estimate proposed by Dai et al. (2009) of ∼32.57 yr. We find the binary mass function of orbit of the tertiary body orbit to be $f(M) = 3.2 \times 10^{-6}$ $M_\odot$. For a combined mass of the two major components of Z Cha of 0.955 $M_\odot$ (McAllister et al. 2019), this leads to a brown dwarf mass of ∼0.015 $M_\odot/\sin i_3$, where $i_3$ is the inclination of the orbital plane of the third body. Assuming our new estimate for the orbital period, a full orbital cycle of the third body in Z Cha has now been sampled, as can be seen clearly in our fit in Fig. 9. This makes Z Cha one of only very few systems for which this has been achieved (see also e.g. Beuermann et al. 2011, for a similar study on the AWD DP Leonis).

However, there are a number of important considerations regarding these results. The time standard[5] employed by prior studies of Z Cha is often unclear during the earlier part of Z Cha's observational history. The use of these alternative time standards can lead to differences of up to ∼50 s in the reported times of eclipse minima (e.g. van Amerongen et al. 1990). In addition to this, the orbital period we calculate for the third body is similar to the length for which Z Cha has been observed, leading to the possibility that our result may be contaminated by windowing effects. Future observations of the O–C behaviour of Z Cha will be able to confirm or refute the presence of such a third body in this system.

### 5.2 Hysteresis in eclipse depth/out-of-eclipse flux space

It is possible to use the eclipse fraction diagrams, shown in Figs 10 and 11, to estimate properties of the eclipses in the Z Cha system. Previous authors have attempted to deconvolve the quiescent eclipses of Z Cha into a series of eclipses of individual components of the system (Wood et al. 1986; McAllister et al. 2019). This technique leads directly to an estimate of the fraction of the disc flux that is eclipsed during eclipse maximum. Previous studies (e.g. Wood et al. 1986; McAllister et al. 2019) find that the accretion disc is only partially obscured at maximum eclipse depth during quiescence. However, we find a 1:1 correlation between eclipse depth and out-of-eclipse flux for Z Cha during quiescence in Sector 6. This suggests that the vast majority of the disc flux is missing during each eclipse at this time, and hence the disc is entirely or almost entirely eclipsed. To estimate the minimum possible size of the accretion disc, we calculate the circularization radius of the disc using the formula (e.g. Frank, King & Raine 2002):

$$R_{\rm circ} = a(1+q)(0.5 - 0.227 \log q)^4 \,, \qquad (2)$$

[5]In this paper, we refer to *TESS*-calculated BJDs, which agree with times calculated using the $BJD_{TDB}$ standard to within 1 s (Bouma et al. 2019).

where $a$ is the semimajor axis of the orbit and $q$ is the mass ratio. Using the values of $q$ and $a$ from McAllister et al. (2019) (see Table 1), we estimate that the minimum accretion disc radius is $\sim$0.170 $R_\odot$. This value is slightly smaller than the red dwarf eclipsor's radius of 0.182 $R_\odot$, also taken from McAllister et al. (2019). As such, the red dwarf in the Z Cha system would be able to totally eclipse the disc if it passes very close to the centre of the disc as seen from the Earth.

Notably, we were not able to fit a well-constrained 1:1 correlation to eclipse depth and out-of-eclipse flux during the quiescent period before the superoutburst. This suggests that the maximum eclipse fraction was significantly smaller before the superoutburst than after it in Sector 6. This in turn suggests that the quiescent disc before the superoutburst had a larger radius than the quiescent disc immediately after the superoutburst. This finding is consistent with the Tidal–Thermal Instability model of superoutbursts (Osaki 1989): in this model, the radius of the accretion disc during quiescence becomes slightly larger after each successive outburst. Eventually, the quiescent disc radius reaches some critical value, and the next outburst triggers a superoutburst, which then resets the quiescent disc radius to some smaller value. As such, the minimum accretion disc radius should occur during the quiescence immediately after a superoutburst, which is consistent with our finding that the disc radius during *TESS* Sector 6 is likely close to the circularization radius.

The increase in luminosity during AWD outbursts is caused by an increase in both the viscosity (and hence temperature) and the size of the accretion disc. Using the presence of the hysteresis in the eclipse fraction diagrams that we show in Figs 10 and 11, it is possible to estimate the sign and magnitude of the response time of the disc to the increase in viscosity or vice versa. Assuming a static accretion disc (e.g. Frank et al. 2002), the temperature $T$ in the disc during outburst as a function of radius $R$ can be expressed as

$$T(R) = \left( k \frac{\dot{M}}{R^3} \left[ 1 - \sqrt{\frac{R_*}{R}} \right] \right)^{\frac{1}{4}} , \tag{3}$$

where $\dot{M}$ is the instantaneous accretion rate, $R_*$ is the radius of the compact object, and

$$k = \frac{3GM}{8\pi\sigma} , \tag{4}$$

which depends only on the mass $M$ of the compact object. Using the Stefan–Boltzmann equation, the luminosity of one side of such an accretion disc between $R_{\rm in}$ and $R_{\rm out}$ is therefore

$$\begin{aligned} L(\dot{M}, R_{\rm out}) &= \frac{1}{2} \int_{R_{\rm in}}^{R_{\rm out}} \sigma 2\pi R T^4(R) \, {\rm d}R \\ &\propto \dot{M} \left( \frac{2\sqrt{R_*}}{3R_{\rm out}\sqrt{R_{\rm out}}} - \frac{1}{R_{\rm out}} + \frac{1}{3R_*} \right) \end{aligned} \tag{5}$$

assuming that the inner disc radius $R_{\rm in} = R_*$ for an AWD. The out-of-eclipse flux from an accretion disc is therefore given by

$$\Phi_{\rm O} \propto L(\dot{m}, r_{\rm disc}) \tag{6}$$

for a disc with radius $r_{\rm disc}$ and instantaneous mass transfer rate $\dot{m}$. First of all, we assume the simplest possible eclipse, in which the star passes directly in front of the centre of the disc as seen from the Earth and the inclination angle of the disc is 90°. The maximum eclipse depth can be estimated as the integrated flux over some region $A_0$ of the disc. $A_0$ can be set equal to the surface of a disc truncated at the radius $r_{\rm ecl}$ of the eclipsing body, unless this is larger than the total flux from the disc:

$$\Phi_{\rm E} \propto \begin{cases} L(\dot{m}, r_{\rm disc}) & \text{if } r_{\rm ecl} > r_{\rm disc} \\ L(\dot{m}, r_{\rm ecl}) & \text{otherwise} . \end{cases} \tag{7}$$

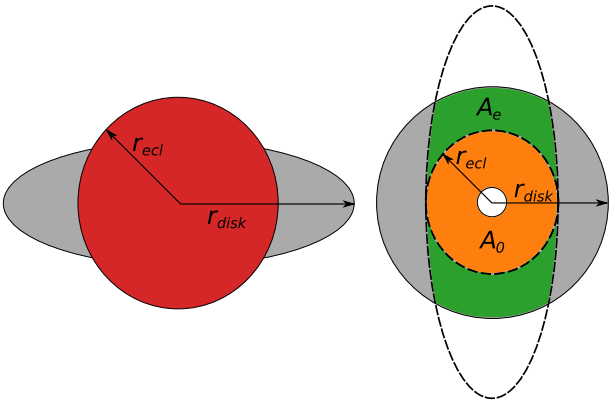


**Figure 14.** The fractional projected area of a sphere (red) on the surface of an inclined disc (grey) is equal to the fractional projected area of an ellipse on to a face-on disc (right), where the eccentricity of the ellipse in the latter case is determined by the inclination of the disc in the former. In our approximation, we assume that the covered region of the disc at peak eclipse ($A_0$ in orange) is equal to a circle with the radius of the eclipser. The true covered region of the disc is $A_{\rm i} = A_0 + A_{\rm e}$, so we underestimate our eclipse depths by a value equal to the integrated flux over $A_{\rm e}$ (in green).

In true astrophysical eclipses, the inclination angle of the disc must be small, and the eclipsed region corresponds to a portion $A_{\rm i}$ of the disc highlighted in Fig. 14. In the limit where the disc radius tends to infinity and its inclination tends to 0°, the factor by which we underestimate the eclipsed area of the disc tends to

$$\frac{A_{\rm i}}{A_0} \xrightarrow{r_{\rm disc}\to\infty,\, i\to 0} \frac{4}{\pi} \frac{r_{\rm disc}}{r_{\rm ecl}} . \tag{8}$$

In the Tidal–Thermal Instability model, the radius of the accretion disc during quiescence cannot exceed the radius of a Keplerian 3:1 resonance with the orbital frequency (Osaki 1989). We estimate a value for this radius in Z Cha to be $\sim$0.33 $R_\odot$, and hence $r_{\rm disc}/r_{\rm ecl} \lesssim 2.2$. As such, our toy model underestimates the eclipsed area of the disc by less than a factor of 3. As the temperature profile of the disc leads to a surface brightness that decreases with increasing $r$, our model underestimates the eclipsed flux from the disc by even less, and our approximation is valid.

Using equations (6) and (7), it is possible to take two signals $\dot{m}(t)$ and $r_{\rm disc}(t)$ and produce the expected eclipse fraction diagrams, up to some constant. We take the case in which $\dot{m}(t)$ and $r_{\rm disc}(t)$ have the same functional form, but $r_{\rm disc}$ instead depends on $t - \phi$ for some constant $\phi$. This way we can model how the eclipse depth diagram would appear for an accretion disc in which an increase in radius lags an increase in accretion rate or vice versa. We show such an eclipse depth diagram for a Gaussian input signal of the form $\dot{m} = A \exp(B(t - C)^2)$ in Fig. 15.

The general behaviour of this modelled eclipse fraction diagram is similar to what we see in the real data from the normal outburst of Z Cha; at low luminosities, eclipse depth and out-of-eclipse flux follow a 1:1 relationship. At some point (labelled **A** in Fig. 15), the radius of the disc significantly exceeds the radius of the eclipsing object, and eclipse depth becomes smaller than out-of-eclipse flux. As the object evolves, it executes a loop in this parameter space below the $x = y$ line, before returning to that line at a point **B**.

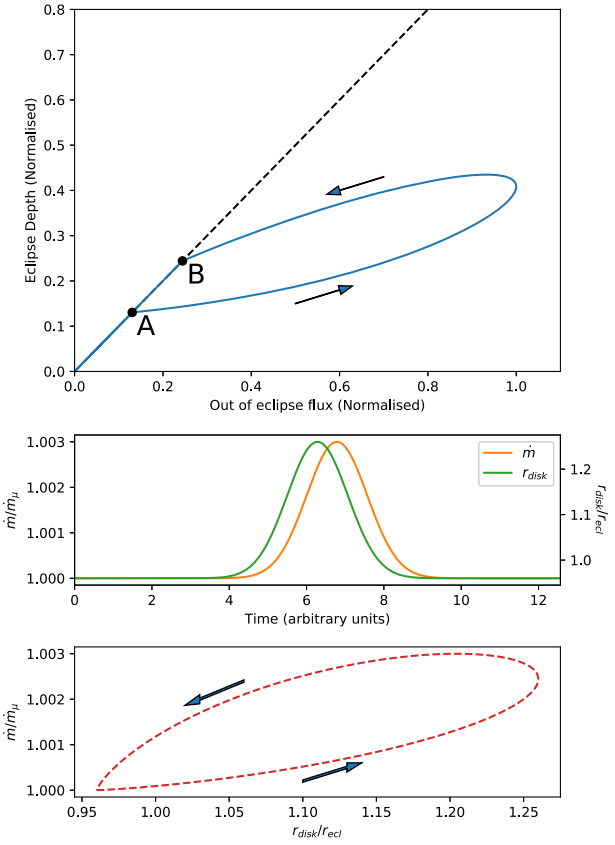


**Figure 15.** Top panel: a plot of eclipse depth against out-of-eclipse flux (an eclipse fraction diagram) for a system modelled using equations (6) and (7), with Gaussian input signals of the form $\dot{m} = A_1 \exp(B_1(t - C)^2)$ and $r_{\rm disc} = A_2 \exp(B_2(t - C - \phi)^2)$. All values have been normalized by the maximum out-of-eclipse flux. In order for the hysteretic loop in this diagram to be executed in an anticlockwise direction (to mimic the data from Z Cha), $-\pi < \phi < 0$. **A** and **B** mark the points in the diagram at which the object leaves and returns to the 1:1 line in this diagram, respectively. Lower panels: plots showing the forms of the input signals $\dot{m}(t)$ and $r_{\rm disc}(t)$ used to generate the top panel. The accretion rate $\dot{m}$ is normalized by the mean accretion rate $\dot{m}_\mu$.

For all input signals, we find that the loop in the eclipse fraction diagram is executed in a clockwise direction if and only if $\phi$ is positive, i.e. the disc radius increases after the instantaneous accretion rate (and disc temperature) increases. Conversely, the loop is executed in an anticlockwise direction if and only if $\phi$ is negative, and the increase in temperature during an outburst lags the increase in disc radius. As we show in Figs 10 and 11, the hysteretic loop in the eclipse fraction diagram is executed anticlockwise in both the outburst and superoutburst of Z Cha, leading us to conclude that the disc begins to increase in size before it increases in temperature in both cases.

This behaviour can also be seen by considering points **A** and **B** in Fig. 15. By definition, at both of these points, $r_{\rm disc} = r_{\rm ecl}$. As the out-of-eclipse flux at **B** is greater than at **A**, it follows that $\dot{m}$ must also be greater at **B** than at **A**. Assuming the functional forms $\dot{m}(t)$ and $r_{\rm disc}(t)$ are similar, this also implies that an increase in accretion rate lags after an increase in disc size. This in turn suggests that, at the onset of an outburst, the increase in viscosity in the accretion disc first causes the disc to expand. The matter in this expanded region of the outer disc then accretes inwards, increasing the mean mass transfer rate within the disc and raising the luminosity of the disc surface.

**Table 4.** A table of best-fitting parameters, in units of phase/cycle, for a parabola fit to the curve traced by the superhump in Fig. 13. $\phi_{\rm SH}$ is the expected phase of the peak of the superhump, and $N$ is the number of cycles since BJD 2458385, the approximate time of onset for the superhumps. $P_{\rm fold} = 0.077\,1892$.

| | $\phi_{\rm SH}(N) = aN^2 + bN + c$ | |
|---|---|---|
| | Value | Error |
| $a$ | $-4.4 \times 10^{-5}$ | $5.0 \times 10^{-7}$ |
| $b$ | $5.5 \times 10^{-3}$ | $7.4 \times 10^{-5}$ |
| $c$ | $3.4 \times 10^{-1}$ | $2.4 \times 10^{-3}$ |

### 5.3 Superhump period and evolution

Our results have implications for the behaviour of a dwarf nova accretion disc during outbursts and superoutbursts, particularly during the onset and the decay of these features. As the brightening events associated with the superhump are large in this system, it is possible to use the path that they trace in a flux-phase plot (e.g. Fig. 13) to estimate how the superhump frequency changes over time. The gradient of a straight line $m$ in a flux-phase plot with the $y$-axis in units of cycles corresponds to an event recurring with a period $P_{\rm SH}$:

$$P_{\rm SH} = P_{\rm fold}\left(\frac{1}{m} + 1\right) = P_{\rm fold}\,(\bar{m} + 1)\,, \tag{9}$$

where $P_{\rm fold}$ is the folding period used to obtain the flux-phase plot and $\bar{m}$ is defined as $1/m$, and is equal to the rate of change of phase as a function of cycle number. Consequently, the rate of change of $P_{\rm SH}$ with respect to time can be calculated as

$$\dot{P}_{\rm SH} = \frac{1}{P_{\rm fold}}\frac{{\rm d}P_{\rm SH}}{{\rm d}N} = \frac{{\rm d}\bar{m}}{{\rm d}N}\,, \tag{10}$$

where $N$ is the time in units of number of cycles since the approximate onset of the superhump at BJD 2458385. By fitting a parabola to the feature caused by the superhump in a flux-phase diagram of the Sector 3 light curve, we find a value $\frac{{\rm d}\bar{m}}{{\rm d}N} = -8.8(1) \times 10^{-5}$, corresponding to $\dot{P}_{\rm SH} = -7.6(1)\,{\rm s\,d^{-1}}$; the best-fitting values for this parabola are given in Table 4, and we plot it in Fig. 13.

At the approximate onset of the superhump, $N = 0$ and, using the values in Table 4 and equation (9), the instantaneous superhump period can be calculated to be 0.077 74(6) d at this time.

The drift in the superhump period can also be investigated using O–C diagrams. To estimate the arrival time of each superhump, we divide the eclipse-removed light curve into segments of 0.077 1892 d, a value close to the approximate median superhump recurrence time. A Gaussian was then fitted to each of these segments to extract the time at which the peak of each superhump occurred. We compared these arrival times against those predicted by a linear ephemeris with a period of 0.077 1892 d; we show the resultant O–C diagram in Fig. 16, showing the quadratic ephemeris corresponding to the parabolic fit to the flux-phase diagram presented in Table 4. To check for consistency, we also fit a quadratic ephemeris to only the superhumps that occurred after the large data gap in Sector 3 (shown in blue in Fig. 16). When extrapolated, this new ephemeris significantly overestimates the O–C values of superhumps that occurred before the data gap (shown in white in Fig. 16). This implies that the mean rate of period decay during and before the data gap was larger than the mean rate of period decay after the data gap. It is therefore unlikely that the superhump period was constant for any significant length of time during this data gap.

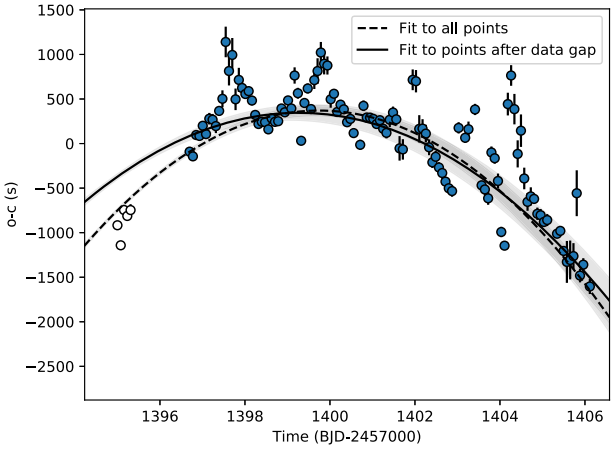


**Figure 16.** An O–C diagram of superhump arrival times against a linear ephemeris with a period of 0.077 1892 d and arbitrary phase. The dashed line is a quadratic ephemeris fit to all superhumps in our sample, corresponding to the quadratic fit to the flux-phase diagram presented in Table 4. The solid line is a quadratic ephemeris fit only to those superhumps that occurred after the large data gap in Sector 3 (in blue). In each case, $1\sigma$ confidence intervals are highlighted in grey. Note that this ephemeris significantly overestimates the O–C values of superhumps that occurred before the data gap (in white).

A decreasing superhump period has been previously noted in a number of other systems (e.g. Uemura et al. 2005). Kato et al. (2009) found that the evolution of the superhump period in most AWD superoutbursts can be described in three evolutionary 'stages':

(i) Stage A, in which the superhump period is high and stable. The superhump period in this stage is higher than in both the other stages.
(ii) Stage B, which occurs after Stage A, in which the superhump period usually decreases smoothly over time. In some sources, the superhump period may increase instead during this stage.
(iii) Stage C, which occurs after Stage B, in which the superhump period is low and stable.

Our results suggest that the superhump period of Z Cha continued to decrease during the data gap in Sector 3. As such, we find that the superhump in the 2018 superoutburst of Z Cha was in evolutionary Stage B for the duration of the observation with *TESS*, and neither Stages A nor C were observed. As the start of the outburst was observed, we are able to state that Stage A did not occur during this superoutburst, but it is unclear whether Stage C occurred as the late stages of the outburst were not observed. Previous studies of the superhump period in superoutbursts of Z Cha (e.g. Kato et al. 2015) have been unable to determine the period derivative during Stage B using O–C fitting techniques. As such our measurement calculated using the flux-phase diagram is, as far as we are aware, the first superhump period derivative calculated for Z Cha.

Stage A superhumps are interpreted as being the dynamic procession rate at the radius of the 3:1 resonance with the binary orbit. Stage B superhumps appear later, when a pressure-driven instability in the disc becomes appreciable. The absence of Stage A superhumps has been noted in a few other SU UMa-type AWDs (e.g. QZ Vir and IRXS J0532, Kato et al. 2009), but the physical parameters that determine whether Stage A superhumps will occur in a given superoutburst remain unclear. Notably, a previous superoutburst of Z Cha in 2014 did show Stage A superhumps (Kato et al. 2015), indicating that the absence of Type A superhumps is a property related to individual superoutbursts rather than to the system.

Additionally, using our estimate of the superhump period at its onset, it is possible to obtain an independent estimate for the mass ratio $q$ of the components of the Z Cha system, where $q$ is the mass ratio defined as

$$q \equiv M_{\rm d}/M_{\rm a}\,, \tag{11}$$

where $M_{\rm a}$ is the mass of the accretor (in this case the white dwarf) and $M_{\rm d}$ is the mass of the donor star. We use the empirical relation between $q$ and $\epsilon$ (Knigge 2006):

$$q = (0.114 \pm 0.005) + (3.97 \pm 0.41) \times (\epsilon - 0.025)\,, \tag{12}$$

where $\epsilon$, the superhump period excess, is a function of superhump period $P_{\rm sh}$ and orbital period $P_{\rm orb}$:

$$\epsilon \equiv \frac{P_{\rm sh} - P_{\rm orb}}{P_{\rm orb}}\,. \tag{13}$$

From equation (12), we thus obtain $q = 0.187 \pm 0.013$. This mass ratio is consistent with recent estimates of $q$ obtained via independent methods (e.g. McAllister et al. 2019).

## 6 CONCLUSIONS

We have performed a study of the timing properties of Z Cha during the *TESS* observations of that source in 2018, as well as a study of how the eclipse properties varied throughout that time period. We calculate the arrival times of eclipses in this system, and use these results to confidently rule out a number of ephemerides constructed by previous studies. We thus create a new orbital ephemeris for the Z Cha system, implying the existence of a third body (consistent with previous studies of this object) and finding a new orbital period for this body of $37.5 \pm 0.5$ yr.

We also study the properties of the 'positive superhump': an oscillation with a period slightly greater than the orbital period, which has been observed during superoutbursts in a number of dwarf nova AWDs. We find that the period associated with the superhump changes significantly during the superoutburst, decreasing towards the orbital period of the system as the superoutburst progresses, and find the rate at which this period decays for the first time in Z Cha. Notably, we find that the superhump in Z Cha evolves in a non-standard way, skipping evolutionary Stage A entirely. Superhumps during previous outbursts of this source have been observed to evolve normally, suggesting that the absence of Stage A evolution is a property of an individual superoutburst rather than of an AWD system.

Finally, we trace how the depth of an eclipse, and the out-of-eclipse flux, varies over the course of both an outburst and a superoutburst. We find that, during quiescence, these parameters follow a 1:1 relationship. Out of quiescence, eclipses deviate from this relationship such that eclipse depth becomes significantly less than out-of eclipse flux. We interpret this as being due to the quiescent disc being comparable in radius to the eclipsing red dwarf, and hence able to be totally or near-totally eclipsed, whereas the disc during outburst becomes larger and is only partially eclipsed. We also find evidence of hysteresis in this parameter space, and show that this can be explained by allowing a lag to exist between an increase in the radius of the accretion disc and the instantaneous mass transfer rate within the disc. We show that this lag is positive, suggesting that the disc first grows in size during an outburst, and then this triggers an increase in the mass transfer rate, which causes a heating of the disc.

## ACKNOWLEDGEMENTS

In this study, we make use of the NUMPY, SCIPY (Jones et al. 2001), and Astropy (Astropy Collaboration 2013) for PYTHON. The figures in this paper were produced using MATPLOTLIB (Hunter 2007) and INKSCAPE (https://inkscape.org).

CK and NCS acknowledge support by the Science and Technology Facilities Council (STFC), and from STFC grant ST/M001326/1. MK is funded by a Newton International Fellowship from the Royal Society. PS acknowledges support by the National Science Foundation (NSF) grant AST-1514737.

## REFERENCES

Applegate J. H., 1992, ApJ, 385, 621
Astropy Collaboration, 2013, A&A, 558, A33
Baptista R., Jablonski F., Oliveira E., Vrielmann S., Woudt P. A., Catalán M. S., 2002, MNRAS, 335, L75
Beuermann K. et al., 2011, A&A, 526, A53
Bianchini A., Mastrantonio E., Canterna R., Stute J., Cantrell K., 2004, A&A, 426, 669
Bond I. A., Freeth R. V., 1988, MNRAS, 232, 753
Bouma L. G. et al., 2019, AJ, **157**, 217
Brinkworth C. S., Marsh T. R., Dhillon V. S., Knigge C., 2006, MNRAS, 365, 287
Cannizzo J. K., Shafter A. W., Wheeler J. C., 1988, ApJ, 333, 227
Cook M. C., 1985, MNRAS, 216, 219
Dai Z., Qian S., Fernández Lajús E., 2009, ApJ, 703, 109
Dai Z.-B., Qian S.-B., Fernández Lajús E., Baume G. L., 2010, MNRAS, 409, 1195
Eastman J., Siverd R., Gaudi B. S., 2010, PASP, 122, 935
Frank J., King A., Raine D. J., 2002, Accretion Power in Astrophysics, 3rd edn. Cambridge Univ. Press, Cambridge
Groot P. J., Augusteijn T., Barziv O., van Paradijs J., 1998, A&A, 340, L31
Han Z.-T., Qian S.-B., Voloshina I., Metlov V. G., Zhu L.-Y., Li L.-J., 2016, Res. Astron. Astrophys., 16, 156
Hellier C., 2001, Cataclysmic Variable Stars. Springer, New York
Honey W. B., Charles P. A., Whitehurst R., Barrett P. E., Smale A. P., 1988, MNRAS, 231, 1
Horne K., 1984, Nature, 312, 348
Hunter J. D., 2007, Comput. Sci. Eng., 9, 90
Irwin A. W., Campbell B., Morbey C. L., Walker G. A. H., Yang S., 1989, PASP, 101, 147
Jones E. et al., 2001, SciPy: Open Source Scientific Tools for Python. http://www.scipy.org/(accessed 2019 July 30)
Kato T. et al., 2009, PASJ, 61, S395
Kato T. et al., 2015, PASJ, 67, 105
Knigge C., 2006, MNRAS, 373, 484
Littlefield C., Garnavich P., Kennedy M., Szkody P., Dai Z., 2018, AJ, 155, 232
Lomb N. R., 1976, Ap&SS, 39, 447
McAllister M. et al., 2019, MNRAS, 486, 5535
Meyer F., Meyer-Hofmeister E., 1984, A&A, 132, 143
Mumford G. S., III, 1969, IAU Circ., 2136, 1
Mumford G. S., 1971, ApJ, 165, 369
Nucita A. A., Kuulkers E., Maiolo B. M. T., de Paolis F., Ingrosso G., Vetrugno D., 2011, A&A, 536, A75
Osaki Y., 1974, PASJ, 26, 429
Osaki Y., 1989, PASJ, 41, 1005
Pilarčík L., Wolf M., Zasche P., Vraštil J., 2018, New Astron., 60, 1
Ramsay G., Cannizzo J. K., Howell S. B., Wood M. A., Still M., Barclay T., Smale A., 2012, MNRAS, 425, 1479
Ricker G. R. et al., 2009, Bulletin of the American Astronomical Sociey, vol. 41, p. 193
Robinson E. L. et al., 1995, ApJ, 443, 295
Scargle J. D., 1982, ApJ, 263, 835
Scaringi S., Groot P. J., Still M., 2013, MNRAS, 435, L68
Uemura M. et al., 2005, A&A, 432, 261
van Amerongen S., Kuulkers E., van Paradijs J., 1990, MNRAS, 242, 522
van Paradijs J., 1983, A&A, 125, L16
Warner B., 1976, in Eggleton P., Mitton S., Whelan J., eds, Proc. IAU Symp. 73, Structure and Evolution of Close Binary Systems. Kluwer, Dordrecht, p. 85
Warner B., O'Donoghue D., 1988, MNRAS, 233, 705
Wood J., Horne K., Berriman G., Wade R., O'Donoghue D., Warner B., 1986, MNRAS, 219, 629
Wood M. A., Still M. D., Howell S. B., Cannizzo J. K., Smale A. P., 2011, ApJ, 741, 105

This paper has been typeset from a TEX/LATEX file prepared by the author.